AIAA JOURNAL
Vol. 35, No. 3, March 1997

Effect of Angle of Attack on Hypersonic Boundary-Layer Stability

Glen P. Doggett* and Ndaona Chokani†
North Carolina State University, Raleigh, North Carolina 27695-7910
and
Stephen P. Wilkinson‡
NASA Langley Research Center, Hampton, Virginia 23681

An experimental investigation of the effects of angle of attack on hypersonic boundary-layer stability on a flared-cone model was conducted in the low-disturbance Mach-6 Nozzle-Test-Chamber Facility at NASA Langley Research Center. Hot-wire anemometry diagnostics were applied to identify the boundary-layer instability mechanisms that lead to transition. The present results show that the boundary layer becomes more stable on the windward ray and less stable on the leeward ray relative to the zero-degree angle-of-attack case. The second-mode instability dominates the transition process at a 0-deg angle of attack; however, on the windward meridian at an angle of attack this mode was stabilized. On the leeward meridian the frequency of the dominant instability was higher than the estimated frequency of the second-mode disturbance; thus the dominant transition mechanism may be other than a second-mode disturbance. Nonlinear effects, such as growth saturation, harmonic generation, and spectral broadening, were observed in the transitional and turbulent flow regimes.

Nomenclature

A	= disturbance amplitude
C_P	= pressure coefficient, $(P - P_\infty)/q_\infty$
F	= frequency, kHz
M	= Mach number
N	= integrated growth factor
P	= static pressure, psia
q	= dynamic pressure, psia
Re_s	= Reynolds number based on surface-arc length and freestream conditions
T	= static temperature, °R
V	= velocity, ft/s
X	= axial distance from model tip, ft
Y	= surface-normal distance, ft
α	= angle of attack, deg
δ	= boundary-layer thickness, ft
λ	= wavelength, ft

Subscripts

∞	= freestream value
o	= reference or stagnation value
gip	= generalized inflection-point value

Introduction

LARGE changes in both heat transfer and skin friction may result from the transition of a hypersonic boundary layer from a laminar to a turbulent state. This transition process is a consequence of the selective amplification and subsequent breakdown of instability waves.[1] Stability experiments seek to validate theoretical and computational methods as well as to improve our understanding of the parameters that influence the transition process. These methods and the improved knowledge are necessary to enable the efficient design of future hypersonic-flight vehicles. Such vehicles usually cruise at some small angle of attack. Thus, a number of experiments have been conducted in a variety of ground test facilities to examine the effects of angle of attack on transition on sharp cones.[2–5] These experiments consistently showed a transition shift downstream on the windward meridian and upstream on the leeward meridian, relative to the 0-deg angle-of-attack case. However, because only the location of transition was documented, no improved knowledge of the phenomena responsible for these trends was gained. This improved understanding can be gained only through stability experiments that document details of the disturbance mechanisms that lead to transition. Stability experiments for a 7-deg half-angle cone tested at 2- and 4-deg angles of attack in a Mach 8 wind tunnel were presented by Stetson et al.[6] In these experiments, hot-wire anemometry techniques were applied to measure the growth of disturbances within the laminar boundary layer. They found that the growth rate of the second-mode disturbances was little affected by angle of attack; however, the characteristics of the disturbances did change. The measured critical Reynolds number increased on the windward meridian and decreased on the leeward meridian, relative to the 0-deg angle-of-attack case.

High-speed test facilities have a measurable freestream disturbance field at high Reynolds numbers. These disturbance fields interact with the model boundary layers, resulting in discrepancies between measurements obtained in different test facilities.[7] This undesirable effect, arising primarily from the acoustic disturbances radiating from the turbulent tunnel-wall boundary layer,[8] established the need for low-disturbance, or quiet, high-speed wind tunnels. The present stability experiments were conducted in a quiet wind tunnel, the Mach-6 Nozzle-Test-Chamber Facility (M6NTC) at NASA Langley Research Center (NASA LaRC). The quiet-tunnel technology developed at NASA LaRC achieves quiet flow by maximizing the region of laminar flow over the nozzle wall.[9] The quiet flow of the M6NTC nozzle has been calibrated in detail[10] and found to be suited for hypersonic boundary-layer stability studies. The primary objective of the present work is to document the effects of angle of attack on the stability of a hypersonic boundary layer on a flared-cone model in a quiet wind tunnel. Surface pressure, surface temperature, and hot-wire measurements are obtained in the windward and leeward meridian planes at 2-deg angle of attack. In addition, as a baseline reference, measurements are also obtained at 0-deg angle of attack. The present study, described in detail elsewhere,[11] is the third in a series of stability experiments[12,13] conducted in the M6NTC at NASA LaRC.

Received July 19, 1996; revision received Nov. 25, 1996; accepted for publication Nov. 26, 1996; also published in *AIAA Journal on Disc*, Volume 2, Number 2. Copyright © 1996 by the American Institute of Aeronautics and Astronautics, Inc. All rights reserved.

*Research Assistant, Department of Mechanical and Aerospace Engineering. Student Member AIAA.
†Associate Professor, Department of Mechanical and Aerospace Engineering. Member AIAA.
‡Research Scientist, Flow Modeling and Control Branch, Fluid Mechanics and Acoustics Division. Senior Member AIAA.

Experimental Method

Test Facility

The Mach-6 axisymmetric quiet nozzle, housed in the M6NTC at NASA LaRC, provided the low-disturbance test environment for the present stability measurements. The nozzle had a throat diameter of 1.00 in. (2.54 cm) and an exit diameter of 7.49 in. (19.02 cm). The length from the throat to the exit was 39.76 in. (100.99 cm). The operating range of stagnation pressures for this nozzle is 80–200 psia (56–141 kPa) with stagnation temperatures of up to 860°R (478 K) attainable. The stagnation conditions for the present tests were $P_{o_\infty} = 130 \pm 2$ psia and $T_{o_\infty} = 810 \pm 3$°R. Under these test conditions the Reynolds number per unit length was $Re/l = 2.82 \times 10^6$/ft. The freestream flow environment of the nozzle has been documented in detail.[10] That study found that for the present test conditions the freestream Mach number measured $M_\infty = 5.91 \pm 0.08$. Furthermore, within the uniform Mach-number envelope, a significant region of quiet flow was identified. Beyond this region, a low-noise zone existed in which the measured disturbances were confined to the 0- to 50-kHz low-frequency band, primarily centered around 16 kHz.

Test Model

The model used in this study, hence referred to as the flared cone, is a 20-in.-long (50.80 cm) sharp-tip cone with a curved-flare afterbody measuring 4.6 in. (11.68 cm) at the base. The first 10-in. (25.40 cm) length of the model measured from the sharp tip is a straight-walled cone with a 5-deg half-angle. The remaining 10-in. (25.40 cm) length of the model is flared outward with a 93.071-in. (236.40 cm) radius of curvature. The purpose of the flare is to generate an adverse-pressure gradient that may promote high-disturbance growth rates on the model within the quiet-flow operating capabilities of the M6NTC facility. The Reynolds number based on freestream conditions and the length of the flared cone was $Re = 4.7 \times 10^6$. The model's highly polished thin-skin construction minimized both surface roughness and heat-conduction effects. The flared cone was sting mounted onto a strut that was placed on precision-machined blocks to position the model at an angle of attack. The precision of the model angle was ± 0.2 deg. The test model was centrally located within the uniform Mach-number envelope of the nozzle with the base of the model 3 in. downstream of the nozzle exit plane inside the open-jet test section.[11]

The effect of the adverse pressure gradient on the stability of the boundary layer on the flared cone at $\alpha = 0$ deg has been studied numerically.[14] This study determined the most-unstable second-mode disturbances to be in the frequency range 235–260 kHz with less-unstable first-mode disturbances in the frequency range 55–70 kHz. Measurement of boundary-layer disturbances in these high-frequency bands should not be affected adversely by the low-frequency, narrow-band facility noise. No stability computations were previously available, however, to estimate the frequency ranges for the angle-of-attack configurations.

Measurements

A conventional schlieren system was used to visualize the flow downstream of the nozzle exit plane over the aft portion of the model. A 1-μs duration spark light source was used. The schlieren knife edge was oriented parallel to the nozzle axis to monitor the positions of the model and nozzle exit shocks.

The flared cone was instrumented with 51 thermocouples axially spaced along a single meridian at 1-in. (2.54 cm) intervals between $X = 2$ in. ($Re_s = 0.47 \times 10^6$) and $X = 9$ in. ($Re_s = 2.12 \times 10^6$) and at 0.25-in. (0.64-cm) intervals from $X = 9$ in. to $X = 19.75$ in. ($Re_s = 4.64 \times 10^6$). Along the opposing meridian, 29 equally spaced static-pressure taps are located. The pressures were measured to within $\pm 5.76 \times 10^{-4}$ psia. The accuracy of the temperature measurements was ± 3°R.

A hot-wire anemometer system was used to obtain mean-flow and stability measurements in the boundary layer. The hot wire was a 0.0001-in.-diam (2.54×10^{-4} cm) platinum-plated tungsten wire spot-welded between two stainless steel broaches. The typical length-to-diameter ratio of the thin-filament hot-wire sensors was 200. The reliability of the hot-wire position with respect to the model surface arc-length distance was ± 0.02 in., and the accuracy of the measured surface-normal distance was estimated to be ± 0.002 in. As a reference scale, the boundary-layer thickness near the base of the 20-in.-long (50.80-cm) model at $\alpha = 0$ deg was about 0.06 in. (0.15 cm).

A constant-voltage anemometer (CVA), described elsewhere,[15] was used to obtain measurements from the single-component hot-wire sensor. The CVA system, with a reported 350-kHz bandwidth, was a prototype and remains under continued evaluation and development. Mangalam et al.[16] have examined the signal-to-noise ratio of the CVA in a hypersonic flow. Comte–Bellot[17] and Kegerise and Spina[18] have examined the static response of the CVA in subsonic and supersonic flows, respectively. An analysis of the dynamic response of the CVA was presented by Sarma.[15] The present measurements, obtained with the CVA system, were not calibrated. However, the sensitivity of the CVA to the mass-flux contribution becomes considerably larger than that to the stagnation temperature contribution as electrical heating of the hot-wire sensor increases.[12,18] Electrical heating of the wire is increased by raising the sensor voltage or current. The present measurements were obtained with the hot-wire sensor operated under such high-voltage, heated-wire conditions. Thus, the dependence of the anemometer output is primarily attributed to the mass-flux contribution.

Experimental Procedure and Data Reduction

The model was tested at angles of attack of $\alpha = 0$ and 2 deg. Baseline measurements were obtained along a single meridian for the $\alpha = 0$ deg case, and angle-of-attack measurements along the windward and leeward meridians for the $\alpha = 2$ deg case.

The hot-wire probe was traversed over 17 streamwise locations in 0.5-in. (1.27 cm) increments along the nozzle axis over the flared region of the model. Fewer stations were surveyed for the windward case. Mean-flow measurements were obtained at 13 discrete locations within the boundary layer at each streamwise location. For mean-flow measurements the time-averaged mean and rms signals were recorded from the CVA system. The mean output qualitatively represented the mean-flow mass-flux profile. The rms output is a measure of the flow-disturbance energy; thus, the peak-rms location identified the locus of maximum disturbance energy. Subsequent stability measurements were obtained at these maximum-energy locations.

The stability measurements were based on time histories of the instantaneous flow-disturbance fluctuations. The time-series data were recorded as follows. The CVA output was first analog filtered with a passband from 1 to 810 kHz to minimize the effects of low-frequency electronic noise and high-frequency aliasing. Then 40,000 data values were digitally sampled at a rate of 2 MHz with an 8-bit numerical precision oscilloscope. The averaged-power spectra then were computed as follows: The sample record was divided into segments of 256 samples. From each segment the mean value of the segment was subtracted. A Hanning window then was applied to the segment, and the fast Fourier transform of the windowed segment was computed with 1024 data points. Power spectra from 156 nonoverlapping segments of the original record were averaged to compute the averaged power spectrum. This procedure was applied to an additional record of 40,000 points recorded at the same location, and these power spectra then were averaged for each measurement location.

The change in the integrated growth factor, the N-factor difference, is given by

$$N - N_o = \ln(A/A_o) \tag{1}$$

where the amplitude spectra A were evaluated by taking the square root of the average power spectra and the arbitrary reference location was taken as the most upstream measurement location. Because of the finite level of noise in the CVA system, the integrated growth factor N is not itself physically measurable, nor is the unknown integrated growth factor at the arbitrary reference location N_o. For the growth to be detected experimentally, the disturbance must have an amplitude greater than the additive noise in the anemometer system. Thus, regions where growth is not experimentally measured should not necessarily be interpreted as regions of stability. Downstream

of measured disturbance growth, the slope of the N-factor difference distribution can be compared on a consistent basis with linear stability theory (LST) predictions.

Navier–Stokes Computations

The mean flow over the flared cone was modeled by the numerical solution of the laminar Navier–Stokes equations using the NASA LaRC-developed code CFL3D. This code has been used to obtain axisymmetric mean-flow solutions on which LST computations were based for the flared cone at $\alpha = 0$ deg in an earlier study.[14] In the present study the flow was computed for the flared cone at $\alpha = 0$ and 2 deg to correspond with the experimental test cases. Additionally, to assess the impact of the precision of the model alignment, the case where $\alpha = 0.2$ deg also was computed. A detailed description of the computational method is given elsewhere.[11]

In addition to providing benchmark pressure and temperature distributions for comparison with surface measurements, the computations also provided a basis for estimating the frequency of the second-mode disturbances. From the computed velocity at the generalized inflection point V_{gip} and the known boundary-layer scaling[19] of the second-mode disturbance wavelength $\lambda_{2nd\ Mode}$, the frequency of a second-mode disturbance was evaluated by

$$F_{2nd\ Mode} = \frac{V_{2nd\ Mode}}{\lambda_{2nd\ Mode}} \approx \frac{V_{gip}}{2\delta} \tag{2}$$

where the boundary-layer thickness δ was estimated from the computed velocity profiles. This frequency estimate is not presented as a substitute for LST computations. Rather, in the absence of available LST computations for the present angle-of-attack cases, this estimate provided a general indication of the range of frequencies that can be measured in the experiments.

Results

The computed pressure contours for the $\alpha = 2$ deg configuration are plotted in Fig. 1a. The scale drawing of the nozzle serves only as a geometric reference; the nozzle itself is not modeled in the computations.[11] The streamwise extent of the CVA hot-wire measurements also is shown. The pressure waves emanating from the flare remain downstream of the shock that originates from the model tip. In the nozzle exit plane, the model shock is 0.5 in. (1.4 cm) away from the nozzle wall on the windward side of the model and 0.3 in. (0.8 cm) on the leeward side. These measurements from the computed data are reliable to within $\pm$0.1 in. ($\pm$0.3 cm). The schlieren images over the leeward and windward portions of the model, shown in Figs. 1b and 1c, respectively, verify that the shock originating from the lip of the nozzle exit does not impinge on the model surface. Because of the limited sensitivity of the schlieren system, the relatively weak model shock is not clearly discernible in the schlieren image. However, in the lower left of the windward schlieren image, the model shock is seen as a dark line running almost parallel to the model surface. The distance from this shock to the nozzle wall in the exit plane is measured to be 0.63 $\pm$ 0.03 in. (1.6 $\pm$ 0.08 cm). The boundary-layer thickness at the nozzle exit can be estimated from the distance between the orifice of the flush-mounted static-pressure tube, at the nozzle exit, to the inner edge of the free shear layer. In the leeward schlieren image, Fig. 1b, this boundary-layer thickness is 0.22 $\pm$ 0.03 in. (0.56 $\pm$ 0.08 cm). It is clear that the model shock exits the nozzle without reflecting from the nozzle wall or interacting with the nozzle wall boundary layer. It is also pertinent to note that the model shock locations estimated from the schlieren images and computations are in good agreement.

Surface Pressure and Temperature

The measured surface-pressure distribution for the $\alpha = 0$ deg baseline case is plotted in Fig. 2a. Also shown are the Navier–Stokes computations for the $\alpha = 0$ and 0.2 deg cases. The constant-pressure region corresponds to the straight-walled cone portion of the model, and the pressure rises steadily along the flare. The estimated variation due to the model alignment is indicated by the envelope of the $\alpha = 0.2$ deg computations. Overall, the agreement between the measurements and the computations is very good. The $\alpha = 2$ deg pressure distributions are plotted in Fig. 2b. These

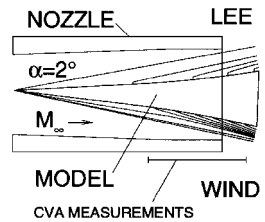

a) Computed pressure contours in windward and leeward planes overlaid on scale drawing of test nozzle

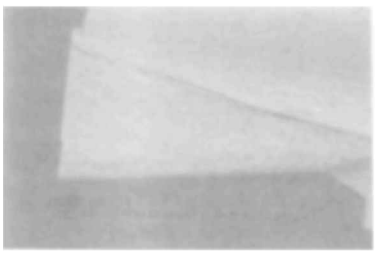

b) Schlieren photograph of leeward plane

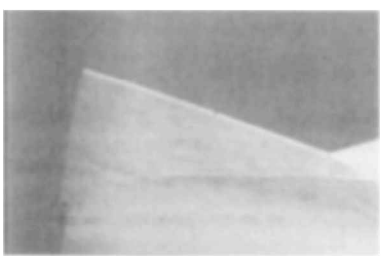

c) Schlieren photograph of windward plane

Fig. 1 Navier–Stokes computations and schlieren visualization for $\alpha = 2$ deg case.

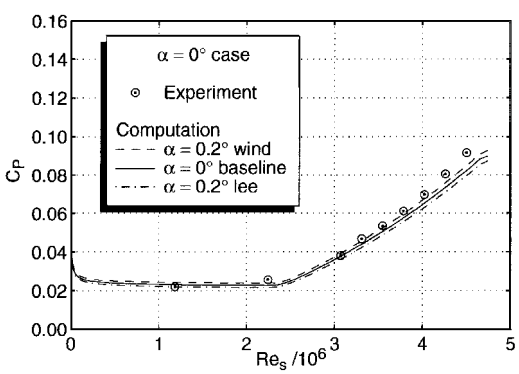

a) $\alpha = 0$ deg baseline case

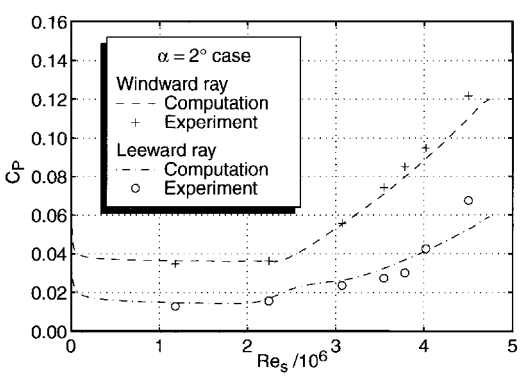

b) $\alpha = 2$ deg windward and leeward cases

Fig. 2 Surface pressure measurements with Navier–Stokes computations.

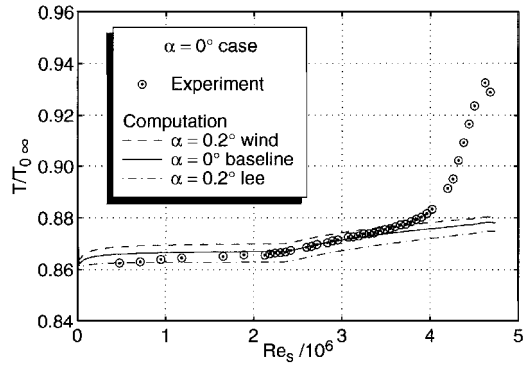

a) $\alpha = 0$ deg baseline case

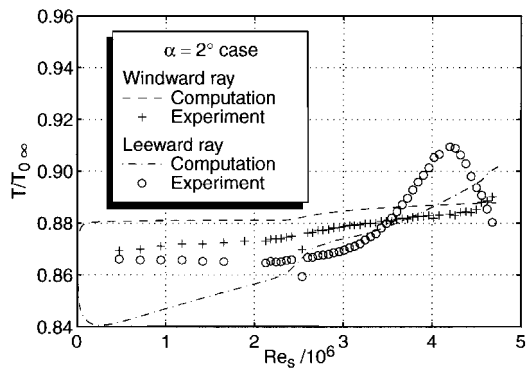

b) $\alpha = 2$ deg windward and leeward cases

Fig. 3 Surface temperature measurements with Navier–Stokes computations.

measurements also show good agreement with the computations along the cone portion. Along the windward meridian, the measured pressure falls just slightly higher than the computed values. The measured leeward distribution, however, shows a more significant deviation from the computed pressure gradient over the flare.

The surface-temperature measurements for the $\alpha = 0$ and 2 deg test cases are shown with the corresponding computations in Fig. 3. The $\alpha = 0$ deg measurements fall within the computed $\alpha = 0.2$ deg envelope up to $Re_s = 3.8 \times 10^6$. Beyond this region, the onset of transition is indicated by the large temperature increase. The location of transition onset, determined by the intersection of two straight lines extended from the laminar and transitional regions, is at $Re_s = 4.2 \times 10^6$. For the $\alpha = 2$ deg case, a greater temperature difference is noted between the windward and leeward meridians in the computations than in the experiment. This discrepancy may be due to thermal conduction between the windward and leeward meridians in the experiment, which is thought to average out temperature differences. The windward measurements, following the trend of the laminar-flow computations, gradually increase toward the base. In contrast, the leeward measurements show a sharp rise due to the transition onset at $Re_s = 3.33 \times 10^6$, which is upstream of that observed in the $\alpha = 0$ deg case.

Mean-Flow Boundary-Layer Profiles

The uncalibrated, normalized mean CVA output voltage is plotted against surface-normal distance Y and streamwise location Re_s in Fig. 4a for the $\alpha = 0$ deg baseline case. The profile shape does not change appreciably in the laminar region. The boundary-layer thickness δ was estimated on the basis of the slope of the mean-profile data refined with a smoothing cubic-spline fit and is shown in the Y—Re_s plane of this three dimensional plot. The adverse-pressure gradient retards boundary-layer growth, as shown by the slight decrease in δ over the flare. Downstream of the transition onset, $Re_s = 4.2 \times 10^6$, the mean profiles broaden and δ increases.

Mean profiles for the $\alpha = 2$ deg windward case are shown in Fig. 4b. The profile shapes maintain their laminar-like shape with a well-defined boundary-layer edge. Also, the δ distribution remains fairly constant with the exception of some experimental scatter. The

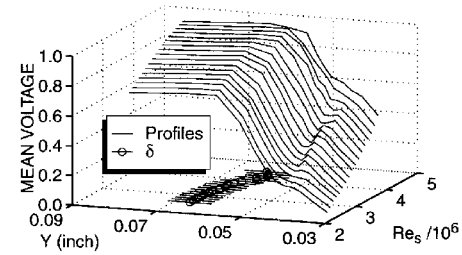

a) $\alpha = 0$ deg baseline case

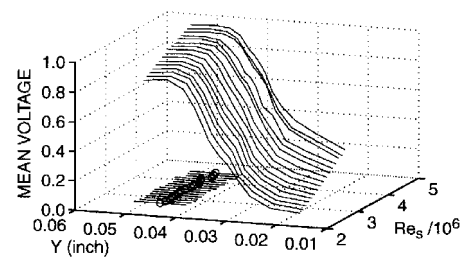

b) $\alpha = 2$ deg windward case

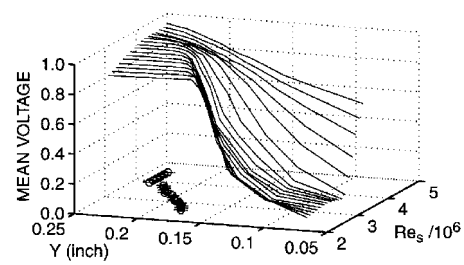

c) $\alpha = 2$ deg leeward case

Fig. 4 Mean-flow boundary-layer profiles.

$\alpha = 2$ deg leeward mean profiles are shown in Fig. 4c. The upstream profiles have a laminar shape; however, as the profiles evolve downstream, their shape fills out. Toward the aft of the flare, the boundary-layer thickness increased beyond the Y range over which hot-wire measurements were obtained.

Boundary-Layer Disturbance-Energy Profiles

The disturbance-energy profiles for the $\alpha = 0$ deg baseline case are plotted in Fig. 5a. These profiles show the development of a localized disturbance within the laminar boundary layer. Downstream of the transition onset, $Re_s = 4.2 \times 10^6$, the disturbance grows in amplitude and broadens in extent. The Y location, where flow disturbances have a peak amplitude (indicated by the circular plot symbols), corresponds to the generalized inflection point[11] and occurs at approximately 85% of the boundary-layer thickness. The rms profiles for the $\alpha = 2$ deg windward case are shown in Fig. 5b. In this case the rms profiles have two maxima. The peak closer to the boundary-layer edge is attributed to the disturbances at the generalized inflection point.[11] The peak closer to the surface results from the increased sensitivity of the hot-wire sensor under decreased mass-flux conditions.[12] The onset of rapid disturbance growth occurs farther downstream than in the baseline case. In contrast, the $\alpha = 2$ deg leeward profiles, presented in Fig. 5c, show disturbance growth farther upstream than in the baseline case; and the disturbance rapidly spreads across the whole boundary layer.

Boundary-Layer Disturbance Spectra

The normalized amplitude spectra $\ell n(A/A_o)$ are plotted for the $\alpha = 0$ deg baseline case in Fig. 6a, where the most-upstream spectrum is used as the reference condition. Significant disturbance growth is clearly observed in the 225- to 325-kHz frequency band, with a peak amplitude at 266 kHz. In the frequency range below 75 kHz, disturbance growth also is detected, but this is mostly indistinguishable from the facility noise in the 0- to 50-kHz band. Additional disturbance growth is detected at the higher-order harmonics of the 266-kHz disturbance at 531 and 797 kHz. The second-mode

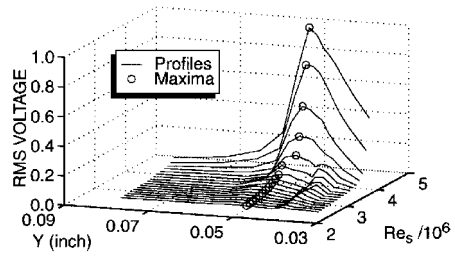

a) $\alpha = 0$ deg baseline case

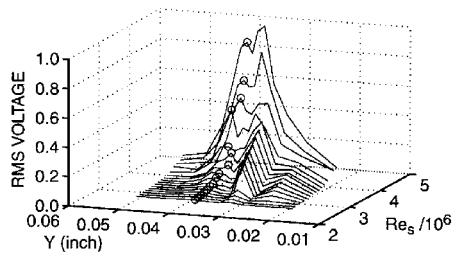

b) $\alpha = 2$ deg windward case

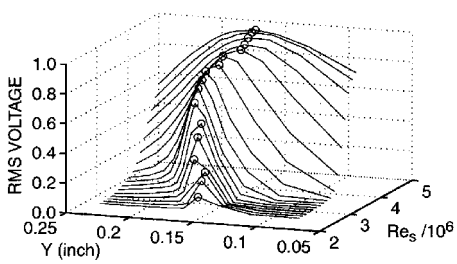

c) $\alpha = 2$ deg leeward case

Fig. 5 Boundary-layer disturbance-energy profiles.

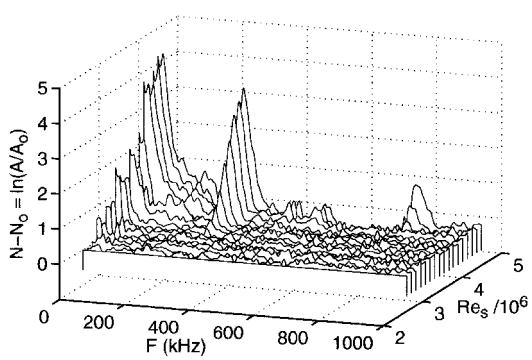

a) Disturbance amplitude spectra

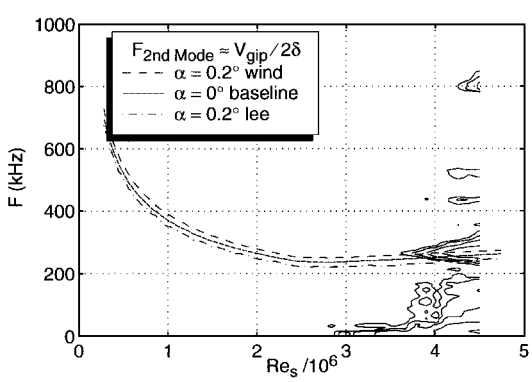

b) Estimated second-mode disturbance frequency with measured *N*-factor contours

Fig. 6 Stability measurements for $\alpha = 0$ deg baseline case.

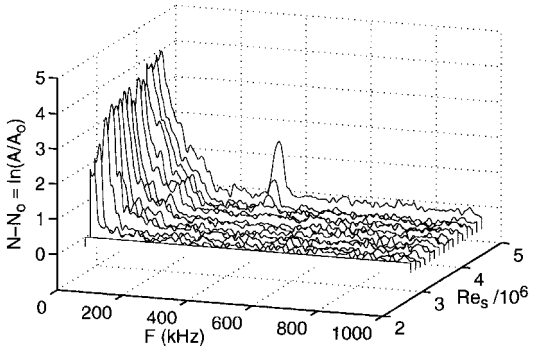

a) Disturbance amplitude spectra

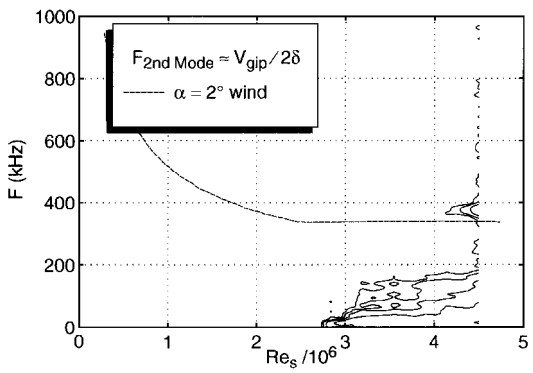

b) Estimated second-mode disturbance frequency with measured *N*-factor contours

Fig. 7 Stability measurements for $\alpha = 2$ deg windward case.

frequency estimates based on the present Navier–Stokes computations are overlaid on a contour plot of the measured *N*-factor spectra in Fig. 6b. The $\alpha = 0$ deg baseline and the $\alpha = 0.2$ deg windward and leeward computations are shown with the $\alpha = 0$ deg data. The computed second-mode frequency decreases along the cone portion of the model as the boundary layer grows. Over the flare where boundary-layer growth is retarded, however, the computed frequency remains fairly constant and falls within 2% of the measured 266-kHz frequency at $Re_s = 4.5 \times 10^6$. Thus, the 266-kHz disturbance is identified as a second-mode disturbance.

Two distinct peaks are observed in the normalized amplitude spectra for the $\alpha = 2$ deg windward case shown in Fig. 7a. The low-frequency peak is identified as facility noise in the 0- to 50-kHz band. The other disturbance is centered at 380 kHz. The computed second-mode disturbance frequency underpredicts this measured frequency by 11% as shown in the composite plot in Fig. 7b. The discrepancy between the measured and computed frequencies may arise because of the limited precision of the model alignment and the limited accuracy of the $\lambda \approx 2\delta$ approximation. Nevertheless, the 380-kHz disturbance also is identified as the second mode.

In contrast to the preceding cases, the spectra for the $\alpha = 2$ deg leeward case, shown in Fig. 8a, indicate that significant disturbance growth occurs at the most-upstream locations, and that growth very likely has already occurred prior to the first measurement location. A localized peak in the amplitude is initially detected at 141 kHz, but subsequently disperses into a more broadband disturbance downstream. The composite plot presented in Fig. 8b shows that the computed second-mode frequency is about 45 kHz at $Re_s = 4.5 \times 10^6$. This mode is not identified clearly from the measured spectra because of the broadband character of the flow disturbances. In addition, the second mode is obscured because its frequency falls within the 0- to 50-kHz facility-noise band. But, because the initial peak amplitude disturbance at 141 kHz falls beyond the second-mode frequency band, the dominant instability for this case is not associated with the second mode.

N-Factor Distributions

The *N*-factor distributions, $(N - N_o)$ vs Re_s, are plotted for selected frequencies in the unstable bands in Fig. 9a for the $\alpha = 0$

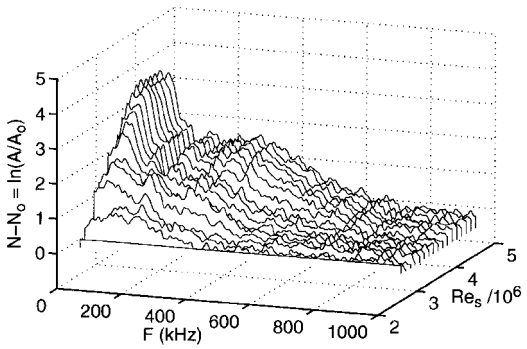

a) Disturbance amplitude spectra

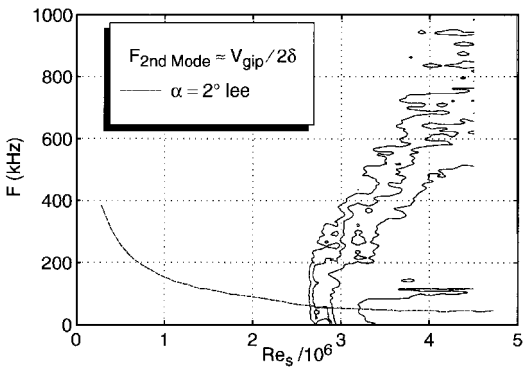

b) Estimated second-mode disturbance frequency with measured *N*-factor contours

Fig. 8 Stability measurements for $\alpha = 2$ deg leeward case.

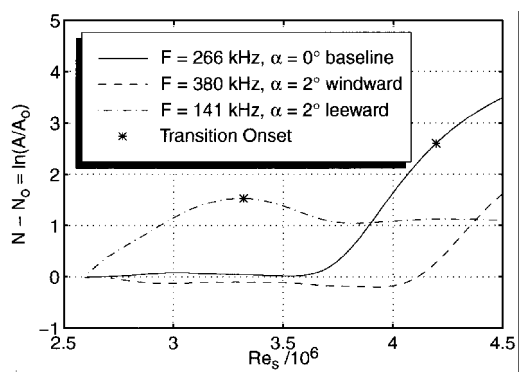

a) Measured distributions for $\alpha = 0$ deg baseline, $\alpha = 2$ deg windward, and $\alpha = 2$ deg leeward cases

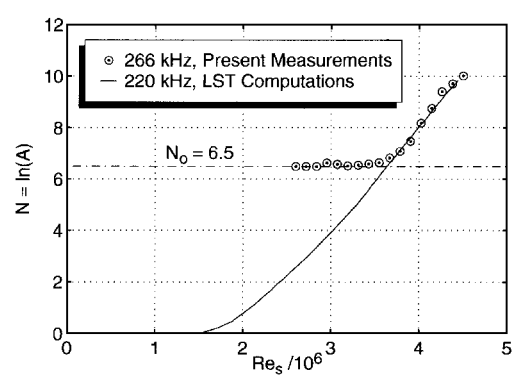

b) Measurements and LST computations[14] for $\alpha = 0$ deg baseline case

Fig. 9 *N*-factor distributions.

and 2 deg cases. These distributions were refined from 17 to 64 streamwise locations by applying a smoothing cubic-spline fit to the raw data. The locations where transition onset is detected are indicated by the asterisks. For the $\alpha = 0$ deg baseline case, the 266-kHz second-mode disturbance was detected initially in the laminar region at $Re_s = 3.65 \times 10^6$. Approximately linear growth of the second mode continues through the transitional region up to the final measurement station, but saturation is not observed. The Reynolds number where the linear growth is detected initially increased to $Re_s = 4.0 \times 10^6$ for the 380-kHz second-mode disturbance in the $\alpha = 2$ deg windward case. In the $\alpha = 0$ deg baseline and $\alpha = 2$ deg windward cases, the zero-slope regions upstream of $Re_s = 3.65 \times 10^6$ and $Re_s = 4.0 \times 10^6$, respectively, indicate that the electronic noise in the CVA system obscures the detection of the flow disturbance. Conversely, in the $\alpha = 2$ deg leeward case, the flat region of the distribution downstream of transition onset indicates that saturation has taken place. In this case, the saturation of the dominant 141-kHz disturbance coincides with the onset of transition at $Re_s = 3.33 \times 10^6$.

Figure 9b shows the $\alpha = 0$ deg baseline case *N*-factor distributions of the second-mode disturbance measured at 266 kHz and of the most-unstable disturbance at 220 kHz from LST computations.[14] The reference value of $N_o = 6.5$ is given by the computed *N* factor at $Re_s = 3.65 \times 10^6$, where the second-mode disturbance is detected initially in the experiment. Upstream of this location, electronic noise in the CVA system obscures the second-mode disturbance. The 20% discrepancy between the measured and computed frequencies may be due to the uncertainty in the alignment angle of the test model, which is ± 0.2 deg. Beyond the transition onset at $Re_s = 4.2 \times 10^6$ the slope of the measured *N*-factor distribution levels off slightly. This deviation from linear growth is accompanied by the appearance of higher-order second-mode harmonics at 531 and 797 kHz.

Concluding Remarks

An investigation of angle-of-attack effects on the stability of the hypersonic boundary layer on a conical model in a low-disturbance facility has been conducted. The freestream Mach number for the present tests was $M_\infty = 5.91$, and the freestream Reynolds number per unit length was $Re/l = 2.82 \times 10^6$/ft. The 5-deg half-angle flared-cone model was tested at angles of attack of $\alpha = 0$ and 2 deg. The flared afterbody was used to generate an adverse-pressure gradient that may induce transition on the model within the quiet-flow operating capabilities of the test facility. Thus, transition occurred on the flared-cone model at a Reynolds number of 4.2×10^6 for the 0-deg case, whereas transition Reynolds numbers in excess of 10×10^6 may occur on straight-walled cones. Despite the uniqueness of the geometry of the flared-cone model, the present data are generally consistent with the angle-of-attack trends observed on straight-walled cones in other investigations, i.e., the onset of transition shifts upstream for the leeward cases, relative to the baseline case, and is delayed for the windward cases.

On the windward meridian, the following observations were made: The boundary layer remained laminar over the length of the model. The frequency of the dominant second-mode instability increased relative to the 0-deg case, scaling with the thinner boundary-layer thickness. In addition, the growth of the second-mode instability was first detected at a larger local Reynolds number.

Along the leeward meridian, transition occurred at a local Reynolds number of 3.33×10^6 for the 2-deg case compared to 4.2×10^6 for the 0-deg case. The coincidence of the transition onset and growth saturation for the leeward case may suggest that the combined effects of adverse-pressure gradient and angle of attack accelerate the process of nonlinear breakdown for the dominant instability on the leeward meridian. Furthermore, because the estimated second-mode frequency was well below the measured frequency of the dominant peak-amplitude disturbance, the dominant instability mechanism on the leeward meridian is thought to be other than a second-mode mechanism.

Acknowledgments

The experimental portion of this work was conducted under NASA Langley Research Center (LaRC) Cooperative Agreement

NCC-1-183. The authors are grateful to William L. Sellers, Branch Head, Flow Modeling and Control Branch, for encouraging this work. Additional support was administered by the North Carolina State University Hypersonic Aerodynamics Program and Mars Mission Research Center funded by Grants NAGW-1072 and NAGW-1331 from NASA Headquarters. The authors would like to acknowledge the engineering technical support of Carol C. Winbush of the Operations Support Division at NASA LaRC in the operation of the M6NTC facility. The authors also acknowledge useful discussions with their colleagues Alan E. Blanchard and Jason T. Lachowicz. The Navier–Stokes computations were performed on the North Carolina Supercomputing Center's Cray T90. The authors are grateful to the reviewers for their constructive comments regarding the manuscript.

References

[1]Stetson, K. F., and Kimmel, R. L., "On Hypersonic Boundary-Layer Stability," AIAA Paper 92-0737, Jan. 1992.

[2]Sheetz, N. W., "Free-Flight Boundary Layer Transition Investigations at Hypersonic Speeds," AIAA Paper 65-127, Jan. 1965.

[3]Stetson, K. F., and Rushton, G. H., "Shock Tunnel Investigation of Boundary Layer Transition at $M = 5.5$," *AIAA Journal*, Vol. 5, No. 5, 1967, pp. 899–906; also AIAA Paper 66-495, June 1966.

[4]Stetson, K. F., "Mach 6 Experiments of Transition on a Cone at Angle of Attack," *Journal of Spacecraft and Rockets*, Vol. 19, No. 5, 1982, pp. 397–403; also AIAA Paper 81-1226, June 1981.

[5]DiCristina, V., "Three Dimensional Laminar Boundary-Layer Transition on a Sharp 8° Cone at Mach 10," *AIAA Journal*, Vol. 8, No. 5, 1970, pp. 852–856; also AIAA Paper 69-12, Jan. 1969.

[6]Stetson, K. F., Thompson, E. R., Donaldson, J. C., and Siler, L. G., "Laminar Boundary Layer Stability Experiments on a Cone at Mach 8, Part 1: Sharp Cone," AIAA Paper 83-1761, July 1983.

[7]Pate, S. R., "Measurements and Correlations of Transition Reynolds Numbers on Sharp Slender Cones at High Speeds," *AIAA Journal*, Vol. 9, No. 6, 1971, pp. 1082–1090; also AIAA Paper 70-799, June 1970.

[8]Laufer, J., "Aerodynamic Noise in Supersonic Wind Tunnels," *Journal of the Aeronautical Sciences*, Vol. 28, No. 9, 1961, pp. 685–692.

[9]Wilkinson, S. P., Anders, S. G., Chen, F.-J., and White, J. A., "Status of NASA Langley Quiet Flow Facility Developments," AIAA Paper 94-2498, June 1994.

[10]Blanchard, A. E., Lachowicz, J. T., and Wilkinson, S. P., "NASA Langley Mach 6 Quiet Wind-Tunnel Performance," *AIAA Journal*, Vol. 35, No. 1, 1997, pp. 23–28; also AIAA Paper 96-0441, Jan. 1996.

[11]Doggett, G. P., and Chokani, N., "Hypersonic Boundary-Layer Stability on a Flared-Cone Model at Angle of Attack," NASA CR-201617, 1996.

[12]Lachowicz, J. T., and Chokani, N., "Hypersonic Boundary-Layer Stability Experiments in a Quiet Tunnel with Bluntness Effects," NASA CR-198272, 1996.

[13]Blanchard, A. E., and Selby, G. V., "An Experimental Investigation of Wall-Cooling Effects on Hypersonic Boundary-Layer Stability in a Quiet Wind Tunnel," NASA CR-198287, 1996.

[14]Balakumar, P., and Malik, M. R., "Effect of Adverse Pressure Gradient and Wall Cooling on Instability of Hypersonic Boundary Layers," High Technology Corp., HTC-9404, Hampton, VA, March 1994.

[15]Sarma, G. R., "Analysis of a Constant Voltage Anemometer Circuit," *Proceedings of the Instrumentation and Measurement Technology Conference*, Inst. of Electrical and Electronics Engineers, New York, 1993, pp. 731–736.

[16]Mangalam, S. M., Sarma, G. R., Kuppa, S., and Kubendran, L. R., "A New Approach to High-Speed Flow Measurements Using Constant Voltage Anemometry," AIAA Paper 92-3957, July 1992.

[17]Comte–Bellot, G., "Hot-Wire Anemometry," *Handbook of Fluid Dynamics*, Oxford Univ. Press, New York, 1995.

[18]Kegerise, M. A., and Spina, E. F., "A Comparative Study of Constant-Voltage and Constant-Temperature Hot-Wire Anemometers in Supersonic Flow," *Proceedings of the Fluids Engineering Division Summer Meeting*, Vol. 4, American Society of Mechanical Engineers, New York, 1996, pp. 297–308.

[19]Mack, L. M., "Stability of Axisymmetric Boundary Layers on Sharp Cones at Hypersonic Mach Numbers," AIAA Paper 87-1413, June 1987.

W. Oberkampf
Associate Editor